

Beam Position Reconstruction for the g2p Experiment in Hall A at Jefferson Lab

Pengjia Zhu^{a,*}, Kalyan Allada^{b,g}, Trent Allison^b, Toby Badman^c, Alexandre Camsonne^b, Jian-ping Chen^b, Melissa Cummings^d, Chao Gu^e, Min Huang^f, Jie Liu^e, John Musson^b, Karl Slifer^c, Vincent Sulkosky^{e,g}, Yunxiu Ye^a, Jixie Zhang^{b,e}, Ryan Zielinski^c

^aUniversity of Science and Technology of China, Hefei, Anhui 230026, China

^b Thomas Jefferson National Accelerator Facility, Newport News, VA 23606, USA

^c University of New Hampshire, Durham, NH 03824, USA

^dCollege of William & Mary, Williamsburg, VA 23187, USA

^eUniversity of Virginia, Charlottesville, VA 22904, USA

^fDuke University, Durham, NC 27708, USA

^gMassachusetts Institute of Technology, MA, 02139, USA

Abstract

Beam-line equipment was upgraded for experiment E08-027 (g2p) in Hall A at Jefferson Lab. Two beam position monitors (BPMs) were necessary to measure the beam position and angle at the target. A new BPM receiver was designed and built to handle the low beam currents (50-100 nA) used for this experiment. Two new super-harps were installed for calibrating the BPMs. In addition to the existing fast raster system, a slow raster system was installed. Before and during the experiment, these new devices were tested and debugged, and their performance was also evaluated. In order to achieve the required accuracy (1-2 mm in position and 1-2 mrad in angle at the target location), new methods were developed for analyzing the data of the BPMs and harps, as well as reconstructing the beam position and angle event by event at the target location. The calculated beam position will be used in the data analysis to accurately determine the kinematics for each event.

¹⁵ *Keywords:* g2p; BPM; raster; beam position

*Corresponding author

Corresponding author: Email address: pzhu@jlab.org, zhupj55@mail.ustc.edu.cn (Pengjia Zhu)

16 **1. Introduction**

17 A polarized ammonia (NH_3) target was used for the first time in Hall A for
18 the g2p experiment [1]. It operated at a low temperature of 1K and a strong
19 transverse magnetic field of either 5 T or 2.5 T. A high electron beam current
20 would cause significant target polarization drop due to target temperature rising
21 and ionization radiation to the target material [2]. To minimize depolarization,
22 the beam current was limited to below 100 nA and a raster system was used
23 to spread the beam spot out to a larger area. The transverse magnetic field
24 in the target region would cause the beam to be deflected downward when the
25 beam enters the target region. To compensate for this, two chicane magnets
26 were placed in front of the target to pre-bend the beam upwards. Due to the
27 low beam current and tight space limitations after the chicane magnets, the
28 experimental accuracy goals for the position (1-2 mm) and angle (1-2 mrad) at
29 the target were challenging to achieve. New beam-line devices and an associated
30 readout electronics system were designed for the g2p experiment to accomplish
31 these goals. Design details and the performance of the beam-line devices will
32 be described in the following sections along with a discussion of a new analysis
method determine the beam position and direction.

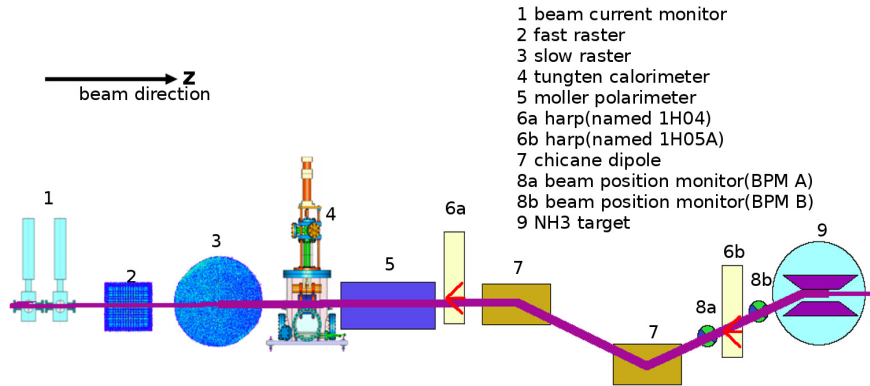


Figure 1: Schematic of beamline components for g2p experiment

34 **2. Beam-line Instrumentation**

35 *2.1. Beam position monitor (BPM)*

36 The scattering angle of the outgoing lepton in deep inelastic scattering, which
37 is defined with respect to the direction of the incident beam, is an important
38 variable for obtaining meaningful physics results. Therefore, the position and
39 direction of the beam, after being bent by the chicane magnetic field and spread
40 out by the rasters, must be measured precisely. Two BPMs and two harps were
41 installed for relative and absolute measurements of beam position and direction
42 near the target, respectively.

43 The BPM consists of four open-ended antennas for detecting the beam po-
44 sition; the measurement is non-invasive to the beam. The BPM chambers
45 shown in Fig.2 are part of the beam pipe. The four antennas are attached
46 to feedthroughs on the interior wall of the pipe at 90° intervals. The BPM

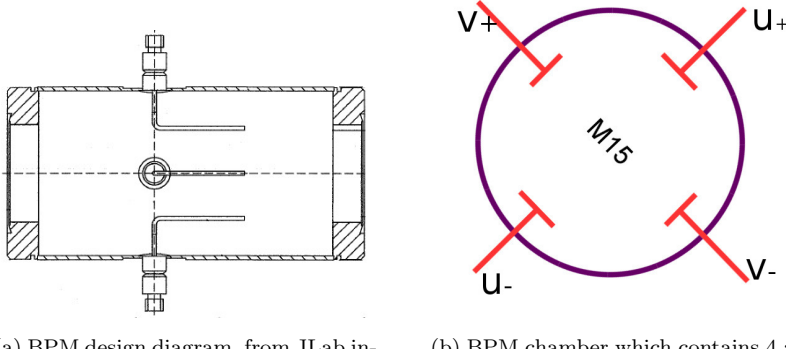


Figure 2: BPM chamber

46
47 chambers are inclined 45° with the global Hall coordinate. In order not to con-
48 fuse with the direction in the Hall coordinate, two antennas are marked as u_+
49 and u_- , which are used to determine the beam position in u direction. An-
50 other two are marked as v_+ and v_- . When the beam passes through the BPM
51 chamber, each antenna receives an induced signal. The BPM front-end receiver

52 collects and sends the signal to the regular Hall A DAQ system and another
53 DAQ system designed for parity violation experiments, the HAPPEX system
54 [3]. The new BPM receiver was designed by the JLab instrumentation group
55 [4] in order to achieve the required precision at a level of 0.1 mm with a beam
56 current as low as 50 nA. The regular DAQ system was connected to a 13-bit
57 fastbus ADC (Lecroy ADC 1881) with an integration time of 50 ns, which was
58 triggered by a scattered electron event. The HAPPEX system was connected
59 to an 18-bit ADC with an integration time of 875 μ s, which was triggered by a
60 beam helicity signal at 1 kHz. The amplitude, A , recorded in the ADC has the
61 following relation with the BPM signal, ϕ :

$$A \propto \phi \cdot 10^{g/20}, \quad (1)$$

62 where g is the gain of the receiver.

63 The BPM receiver generates a large time delay for the output signals. The
64 digital filter used in the receiver contributes 1/175 s delay time, which was the
65 inverse of the bandwidth setting chosen for the filter. There is a $\sim 4 \mu$ s delay
66 as a result of finite processing times. The BPM can not provide event by event
67 position because of this time delay, due to the 25 kHz fast raster system.

68 Because of the space limitation between the second chicane magnet and the
69 target, the two BPMs were placed close to each other. One was placed 95.5 cm
70 upstream of the target while the other was placed 69 cm upstream, making the
71 distance between them only 26.5 cm. The short distance magnified the position
72 uncertainty from the BPMs to target.

73 2.2. Super harp

74 Two super harps were designed and installed in the beam-line, as shown in
75 Fig.1 (label 6a - 1H04 and 6b - 1H05A), to provide an absolute measurement
76 of the beam position for calibration of the BPMs. The new harps were able to
77 work in pulsed beam (1% duty factor) with a current of several μ A. A diagram
78 for the harp is shown in Fig.3,

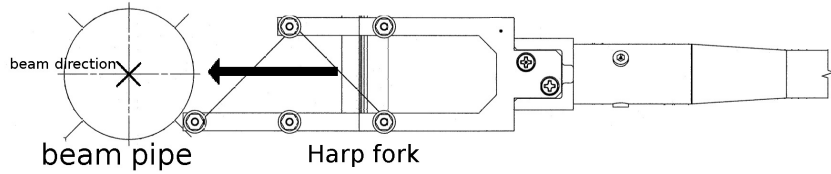


Figure 3: Harp diagram

79 which consists of three wires with a thickness of $50 \mu\text{m}$, a fork and a controller
 80 chassis. The harp chamber is perpendicular to the beam pipe and connected
 81 to the beam pipe as part of the vacuum chamber of the beamline. The two
 82 harps have different configurations of three wires: vertical(|), bank left(\), and
 83 bank right(/) for 1H04, and /, |, \ for 1H05. The angle of the / or \ wires is
 84 45° relative to the wire dock frame. The wires are arranged in a fork (Fig.3)
 85 controlled by a step motor [5] which can be moved in and out of the beam-line.
 86 The harps must be moved out of the beam-line when production data is being
 87 taken because they are invasive to the beam. The original position of the wires
 88 was surveyed before the experiment at a precision level of 0.1 mm . As the motor
 89 driver moved the fork through the beam, each wire received a signal, which was
 90 recorded for further analysis. The signals received from the wire and the step-
 91 counters from the motor driver were then sent to an amplifier and the DAQ.
 92 The amplification and the speed of the motor were adjustable for the purpose
 93 of optimizing the signals of each scan. Recorded data combined with the survey
 94 data was used to calculate the absolute beam position.

95 The signal from the | wire ($\text{peak}_{|}$) was used for getting the x position (x_{harp})
 96 of the beam , and the signals from the /, \ wires ($\text{peak}_{/}$ and peak_{\backslash}) were used
 97 for getting the y position (y_{harp}):

$$\begin{aligned}
 x_{\text{harp}} &= \text{survey}_{|} - \text{peak}_{|} \\
 y_{\text{harp}} &= \frac{1}{2}[(\text{survey}_{\backslash} - \text{survey}_{/}) - (\text{peak}_{\backslash} - \text{peak}_{/})]
 \end{aligned} \tag{2}$$

98 *2.3. Raster system*

99 In order to minimize the depolarization, avoid damage to the target material
100 from radiation, and reduce systematic error for the polarization measurement
101 by NMR (The polarization of the NH_3 target was measured by a NMR coil
102 which installed inside the target cell [6]. The non-uniformity of depolarization
103 could reduce the precision of the NMR measurement due to the measurement
104 being an average over the target), two raster systems were installed at ~ 17 m
105 upstream of the target, as shown in Fig.1 (labels 2 and 3 for fast and slow rasters,
106 respectively). Both the fast and slow rasters consist of two dipole magnets. The
107 same triangular waveforms with frequency of 25 kHz were used to drive the
108 magnet coils of the fast raster to move the beam in x and y directions, forming
109 a rectangular pattern of $2\text{ mm} \times 2\text{ mm}$, as shown in Fig.4.

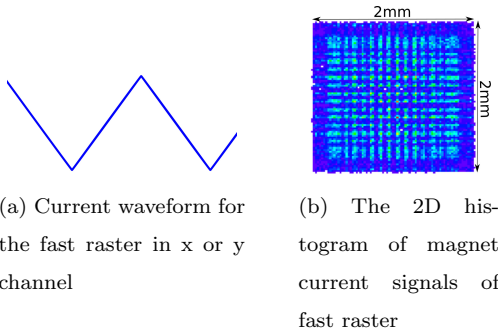


Figure 4: Fast raster pattern

109
110 A dual-channel function-generator¹ was used to generate two independent
111 waveforms to drive the magnet coils of the slow raster. The waveforms for the
112 x and y directions are:

¹agilent 33522A function generator, <http://www.home.agilent.com/en/pd-1871286-pn-33522A/function-arbitrary-waveform-generator-30-mhz>

$$\begin{aligned} x &= A_x t^{1/2} \sin(\omega t), \\ y &= A_y (t + t_0)^{1/2} \sin(\omega t + \phi), \end{aligned} \quad (3)$$

113 where the A_x and A_y are the maximum amplitude, t_0 and ϕ are the AM and
sin phase difference between x and y waveform, respectively. Both of them

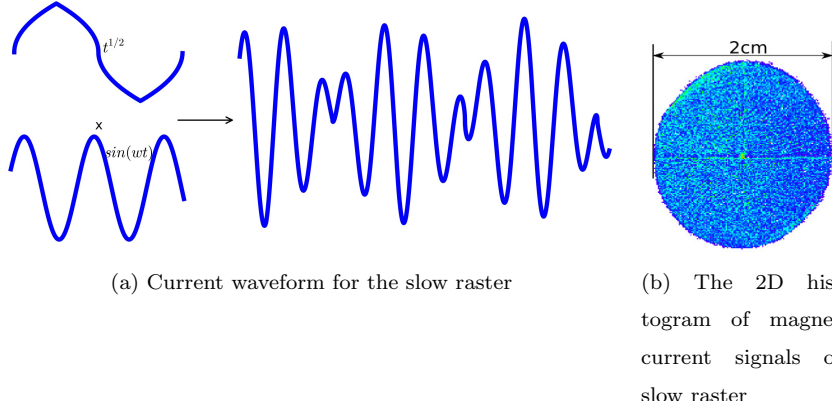
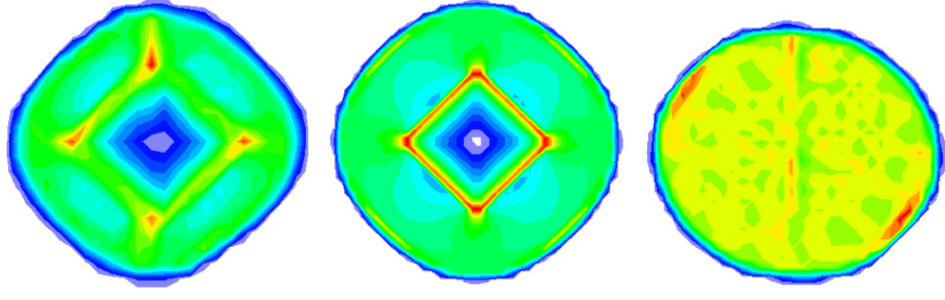


Figure 5: Slow raster pattern

114
115 are sine functions modulated by a function $t^{1/2}$ in order to generate a uniform
116 circular pattern [7], as shown in Fig.5. The frequency of the x and y waveforms
117 kept same: $\omega = 99.412$ Hz. In order to cycle the amplitude modulation (AM)
118 function, four piece-wise functions are combined together. The first term is $t^{1/2}$,
119 and the second term is $period - t^{1/2}$, and so on for the third and fourth terms.
120 The cycled function has the frequency of 30 Hz.

121 The ϕ was locked to $\frac{\pi}{2}$ by the function generator, while the t_0 was manually
122 adjusted to 0. Non-zero t_0 could cause a non-uniformity pattern, as shown in
123 Fig.6(a), which would cause non-uniformity beam distribution. A simulation
124 was reproduced the non-uniformity by setting the t_0 to non-zero, as shown
125 in Fig.6(b). The t_0 was carefully adjusted and minimized before production
126 data taking to avoid the non-uniformity. The pattern of the spread beam was
127 relatively uniform after this adjustment during the experiment, as shown in
128 Fig.6(c).



(a) Raster pattern with $t_0 \neq 0$ (b) Simulated raster pattern, (c) Manually adjust t_0 to 0 with $t_0 \neq 0$

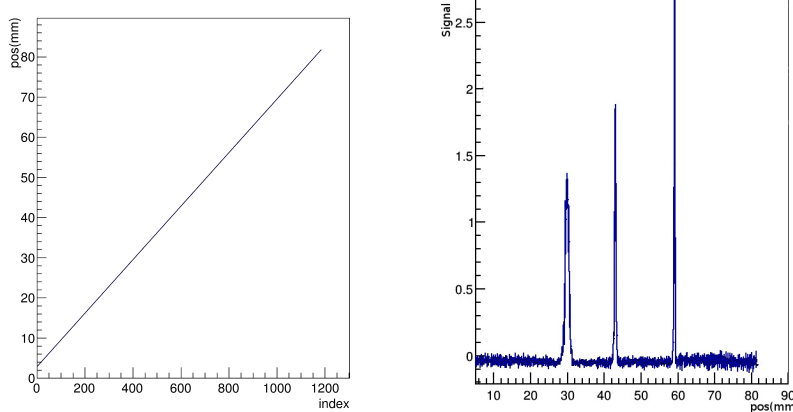
Figure 6: None-zero t_0 caused slow raster non-uniformity, (a) and (c) are from the data, (b) is simulated.

129 3. Data analysis

130 3.1. Harp scans for measuring absolute beam position

131 An example of a harp scan result is shown in Fig.7. There are three groups of
132 recorded data for each harp scan, which are “index”, “position”, and “signal”.
133 The index is related to the moving steps of the fork during the scan. Each
134 step of the index increases by 0.008-0.07 mm depending on the speed of the
135 motor driver [5]. The position is the wire location for each index. The testing
136 results show a good linear relation between the position and the index as shown
137 in Fig.7(a), because the motor speed is uniform. The line is the fitted result
138 with $pos = a * index + b$. According to this linear relation, interpolation or
139 extrapolation can be applied when a few data points are missing, in some cases.
140 The strength of signal vs. position is plotted in Fig.7(b). Each peak represents
141 the location when one of the three wires passed through the beam.

142 The positions measured by the two harps were used for calibrating the beam
143 positions in the two BPMs. When the chicane magnets were on, beam did not
144 pass straight through from the first harp to the second harp. BPM calibrations
145 using two harps were only possible when the chicane magnets were off, i.e. in the
146 straight-through settings. Since the BPM was calibrated in the local coordinate



(a) position vs index for harp scan, used for extending position record

(b) Signal vs position for harp, x axis is position, y axis is the strength of signal. The unit of signal strength is the ADC unit.

Figure 7: 1H05A harp scan data

147 system, the calibration constants were independent from the settings of other
 148 instruments. To make sure that the calibration constants for the BPMs were
 149 still valid during the non-straight-through settings, the settings for the BPM
 150 receiver were kept the same as in the straight-through settings during production
 151 running.

152 The scan data from the harps was not reliable when the current of CW beam
 153 (100% duty factor) was lower than 100 nA due to the low signal-to-noise ratio.
 154 The harp scans were taken in pulsed mode at a current of a few μ A, while the
 155 BPMs were used for production data taking in CW mode at a beam current
 156 of 50-100 nA. For a BPM calibration run, a harp scan was done first in pulsed
 157 mode, then a DAQ run was taken immediately to record the ADC value in CW
 158 mode without changing the beam position. The harp scan was then taken again
 159 in the pulsed mode to double check the beam position. The harp scan data was
 160 discarded and the scan was taken again if the beam position changed.

161 3.2. BPM data analysis and calibration

162 The traditional difference-over-sum (diff/sum) method to calculate the beam
 163 position has the non-linearity effect in the position far away from the center of
 164 the beam pipe [8]. It is necessary to correct the equation of diff/sum since we
 165 have a slow raster. With the assumption of the infinitely long chamber and the
 166 negligible antenna influence for the electric field inside the chamber, the signal
 167 from each antenna excited by the beam can be calculated via image charge
 168 method (Fig. 8) [9, 10] :

$$\phi_i = \phi_0 I \frac{R^2 - \rho^2}{R^2 + \rho^2 - 2R\rho\cos(\theta_i - \theta_0)}, \quad (4)$$

169 where ϕ_i is the signal received in the antenna, and i is u_+ , u_- , v_+ and v_- ,
 170 respectively, ϕ_0 is a constant related to the geometry of the BPM-chamber and
 171 the output resistance, I is the beam current, R is the radius of the BPM vacuum
 172 chamber, ρ is the radial position of the beam, and $\theta_i - \theta_0$ is the angle difference
 173 between the antenna and the beam in the polar coordinate .

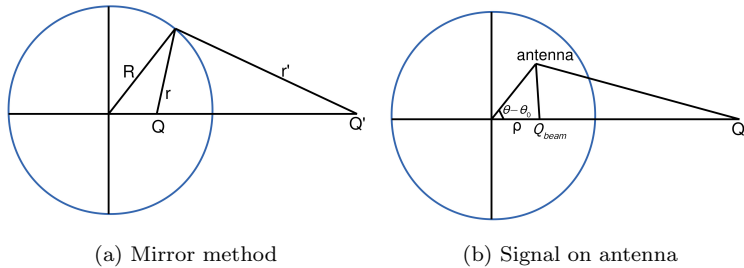


Figure 8: Signal for each antenna of BPM

173
 174 In order to extract the beam position information, and eliminate the de-
 175 pendence on the beam current in equation (4), the diff/sum method is used as
 176 follows:

$$D_U = \frac{\phi_{U+} - \phi_{U-}}{\phi_{U+} + \phi_{U-}}, \quad (5)$$

177 where U is u and v , respectively. Substituting equation (4) into equation (5),
 178 they can be rewritten as follows:

$$D_U = \frac{\phi_{U+} - \phi_{U-}}{\phi_{U+} + \phi_{U-}} = \frac{2}{R} \frac{\rho \cos(\theta - \theta_0)}{1 + \frac{\rho^2}{R^2}} = \frac{2}{R} \frac{U}{1 + \frac{\rho^2}{R^2}}, \quad (6)$$

179 where $\rho^2 = u^2 + v^2$. When $u^2 + v^2 \ll R^2$, equations (6) can be simplified as:

$$U \approx \frac{R}{2} D_U = \frac{R}{2} \frac{\phi_{U+} - \phi_{U-}}{\phi_{U+} + \phi_{U-}}. \quad (7)$$

180 Equation (7) can be used in the simple case when the beam is near the center
 181 of the beam pipe. When the beam is far from the center, equation (7) is no
 182 longer valid. For the g2p experiment, the beam was rastered to have a diameter
 183 of about 2 cm at the target. From equation (6) the beam position can be
 184 calculated as:

$$U = RD_U \left(\frac{1}{D_u^2 + D_v^2} - \frac{1}{\sqrt{D_u^2 + D_v^2}} \sqrt{\frac{1}{D_u^2 + D_v^2} - 1} \right). \quad (8)$$

185 To verify this corrected equation, a simulation was performed. First, a set
 186 of position data was generated (Fig.9(a)), and the designed radius for the BPM
 187 chamber was used for R . Using equation (4) to get the signal for each antenna,
 188 and setting ϕ_0 and I to be equal to 1, equations (8) and (7) were used to
 189 calculate the beam position for comparison. The results are shown in Fig.9(b)
 and 9(c), respectively.

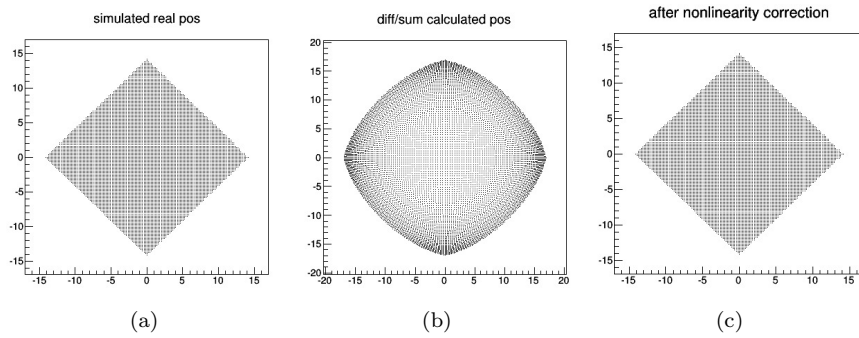


Figure 9: Comparing the calculated results using equation (7) and (8) with simulated position.
 (a) Simulated position; (b) The calculated result with equation (7), (c) The calculated result with equation (8).

190

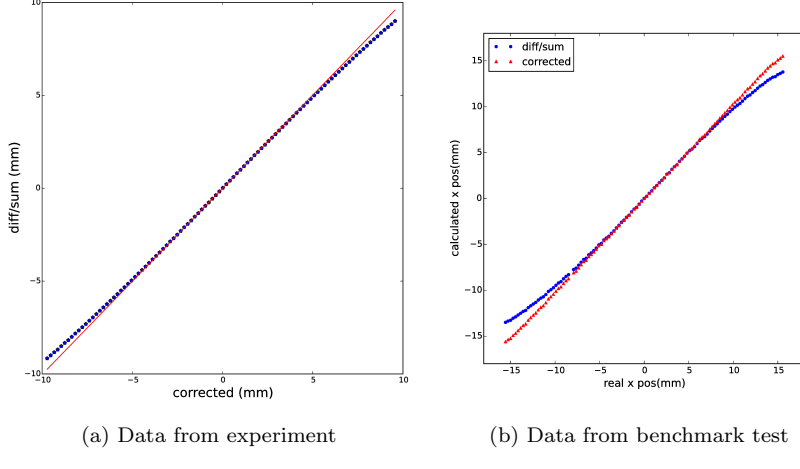


Figure 10: BPM non-linearity correction. (a) Relationship between the position calculated from diff/sum equation (6) (y axis) and the one from corrected equation (8) (x axis). Red solid line is a reference line came from linear fit for the center points . Data is collected from experiment. (b) Comparison between the diff/sum equation (6) and the corrected equation (8) using the benchmark test data. The x axis is the real beam position. The red triangles are the positions calculated from corrected equation (8). The blue circles are the positions calculated from diff/sum equation (6) .

191 The corrected equation is also tested by using the experiment data and
 192 the benchmark test data. Fig.10(a) shows the difference between the position
 193 calculated from the corrected equation (8) and the one from the diff/sum equa-
 194 tion (6). Fig.10(b) shows the comparison with the real beam position from the
 195 benchmark test data. In this way the method using equation (8) can correct the
 196 non-linearity effect caused by the diff/sum method. The handling of the BPM
 197 information which only used for the center beam position (discussed in chapter
 198 3.4) also reduced this non-linearity effect.

199 The final information recorded in the data-stream was designed to have a
 200 linear response with the raw signal in the 50-100nA current range. The ϕ_i in
 201 equation (6) can be rewritten as:

$$\phi_i = a_i(A_i - A_{i_ped} + b_i), \quad (9)$$

202 where A_i and $A_{i,ped}$ are the recorded ADC value and pedestal value, and a_i and
 203 b_i are the slope and intercept of the relationship between ϕ_i and $A_i - A_{i,ped}$.
 204 Equation (7) can be rewritten as:

$$D_U = \frac{(A_{U+} - A_{U+,ped} + b_{U+}) - h_u(A_{U-} - A_{U-,ped} + b_{U-})}{(A_{U+} - A_{U+,ped} + b_{U+}) + h_u(A_{U-} - A_{U-,ped} + b_{U-})}, \quad (10)$$

205 where $h_u = a_{U-}/a_{U+}$, and is related to the ratio of the signals for the U_+ and
 206 U_- antennas and the gain settings of the two channels.

207 Combining the equation (9) and (4), the calibration constant b_i was obtained
 208 by taking the linear fit between the ADC values of BPM and the beam current
 209 with a group of runs with the same beam position but different values of beam
 current: $I \propto (A_i - A_{i,ped} + b_i)$. Figure 11 shows the $A_i - A_{i,ped}$ versus the beam

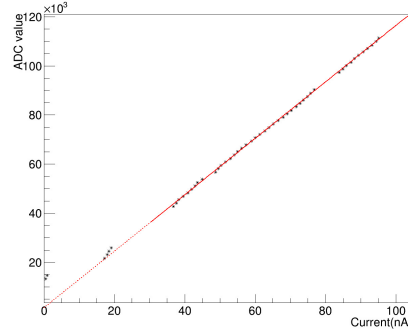


Figure 11: ADC value of BPM raw signal ($A - A_{ped}$) V.S. current

210
 211 current. It can be seen that the ADC values were linear with beam current in
 212 the considering current range of 50-100 nA. The intercept from the linear fit of
 213 Fig.11 is the value b_i .

214 By transporting the position x_{harp} and y_{harp} in equation (2) from two harps
 215 to the BPM local coordinate u_{harp} and v_{harp} , a fit between the BPM data U
 216 and the harp data U_{harp} determined three calibration constants c_0 , c_1 and c_2 :

$$U_{harp} = U_c = c_0 + c_1 u + c_2 v, \quad (11)$$

²¹⁷ where U_c is the calibrated BPM position. It was converted to Hall coordinate X_c
²¹⁸ for further transporting to the target location. An calibration example is shown
in Fig. 12. The asterisks in Fig. 12 represent U_{harp} , and the dots represent U .

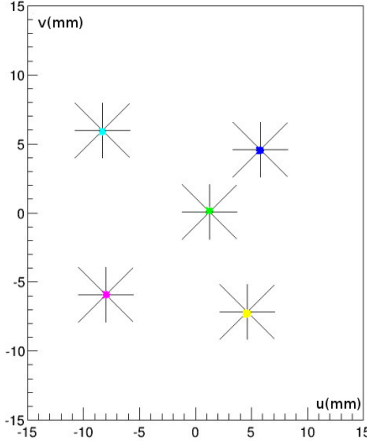
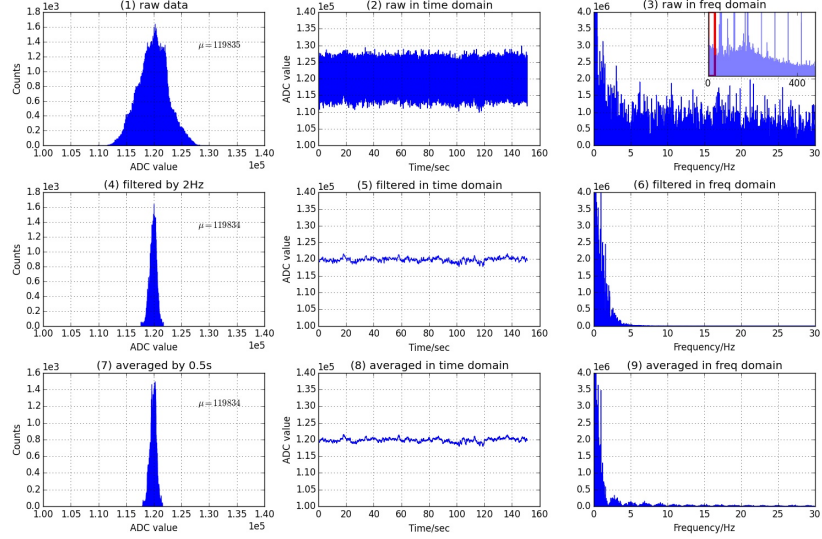


Figure 12: Harp scan data combined with BPM data, the asterisks are the positions from harp, while the dots are from BPM.

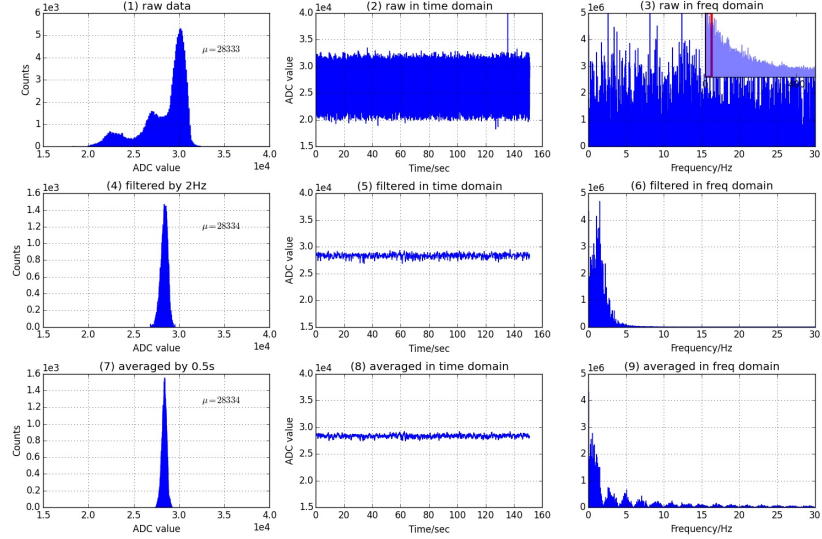
²¹⁹
²²⁰ In order to reduce the noise and improve the resolution during data analysis,
²²¹ a software filter was applied. Since the 18 bit ADC was triggered by the helicity
²²² signal with a fixed frequency, it could be regarded as a sampling ADC. Fig.13
²²³ shows the signal dealt with a 2 Hz low pass filter. The bottom 3 plots in Fig. 13
²²⁴ (a,b) are the averaged signal for comparing with the filtered signal. The average
²²⁵ procedure lead to the same result as the filter. The filter also erases the beam
²²⁶ displacement caused by the rasters, which is necessary to extract the position
²²⁷ of the beam center.

²²⁸ 3.3. Beam position reconstruction at the target

²²⁹ It is easy to transport the position from the BPMs to the target by using a
²³⁰ linear transportation method for the straight through setting. For the settings
²³¹ with a transverse magnetic field at the target, the linear transportation method
²³² can not be used since the beam is bent near the target. A simulation package
²³³ was constructed to simulate the behavior of the beam. Polynomial curve fittings



(a) Normal run with beam



(b) Pedestal run without beam

Figure 13: Software filter applied to BPM signal. (a) is the signal with beam, (b) is the pedestal signal without beam. (1,2,3) in (a,b) are the raw signal without applying the filter, (4,5,6) are applied a 2Hz finite-impulse-response filter with 4th order. (7,8,9) are averaged with 0.5 s. (1,4,7) are the signal's 1-D histogram, (2,5,8) are the signal in time domain, (3,6,9) are in frequency domain. Note all of the plots in (a) is for a single signal, same as in (b).

²³⁴ were used for simulated data to generate the transport functions in order to
transport the beam from the two BPMs to the target (Fig.14).

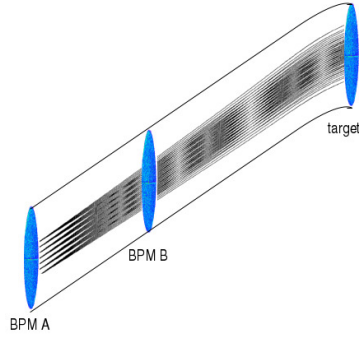


Figure 14: Transporting beam position from BPM to target with transverse target magnet field

²³⁵

²³⁶ A target magnet field map [11] was generated from the TOSCA model. To
²³⁷ test the accuracy of the TOSCA model, the target magnet field was measured
²³⁸ before the experiment [12, 13]. The generated field map was used in the simula-
²³⁹ tion. An event generator generated thousands of electrons with different initial
²⁴⁰ positions and angles, with the energy of the electrons set to the same values as
²⁴¹ in the experiment. The Runge-Kutta method² with 0.02 mm step length was
²⁴² used to generate the trajectories from BPM A to the target by using the field
²⁴³ map. Data extracted from the simulation was used as input for the polynomial
²⁴⁴ fitting:

$$\begin{bmatrix} x_{tgt} \\ y_{tgt} \\ \theta_{tgt} \\ \phi_{tgt} \end{bmatrix} = F \left(\begin{bmatrix} x_{BPMA} \\ y_{BPMA} \\ x_{BPMB} \\ y_{BPMB} \end{bmatrix} \right), \quad (12)$$

²⁴⁵ where F is the fitted polynomial transport function. The positions at the BPMs:
²⁴⁶ x_{BPMA} , y_{BPMA} , x_{BPMB} , y_{BPMB} , and the position and angle at the target:

²http://en.wikipedia.org/wiki/Runge–Kutta_methods

247 x_{tgt} , y_{tgt} , θ_{tgt} , ϕ_{tgt} , are extracted from the simulated trajectory. In total, 24
248 different fits were taken for 4 different target positions and 6 configurations
249 with different target magnetic field and beam energy settings. The validity
250 of the transport functions was explored in the simulation using a new set of
251 random trajectories generated in the same manner as those used in the fitting.
252 The deviation between the fitted transport function and the simulation was less
253 than 0.1%.

254 The transport functions were only used to transport the beam center position
255 from the two BPMs to the target by applying the 2 Hz filter, which filtered out
256 the fast raster and slow raster motion to keep only the beam center position.
257 The transported position were expressed as X_{center} .

258 *3.4. Determining the beam position event-by-event*

259 The readout of the magnet current for the two rasters was connected to
260 a series of ADCs. Two scintillator planes in the HRS form a DAQ trigger.
261 This pulse signal triggered the ADC to record the raster magnet current for
262 each event. The information from the rasters and the BPMs was combined
263 to provide the beam position event-by-event. The position at the target was
264 determined as:

$$X = X_{center} + X_{fstraster} + X_{slraster}, \quad (13)$$

265 where $X_{fstraster}$ and $X_{slraster}$ were the position displaced by the fast raster
266 and slow raster, respectively, which were converted from the current values of
267 the two raster magnets. The calibration of the conversion factors between the
268 magnet current of the rasters and the displaced position will be discussed in the
269 next subsection. An example of reconstructed beam position is shown in Fig.
270 15.

271 *3.4.1. Conversion factor for the slow raster*

272 Two methods were used to calibrate the conversion factor for the slow raster.
273 The first method used the calibrated BPM information, i.e., comparing the

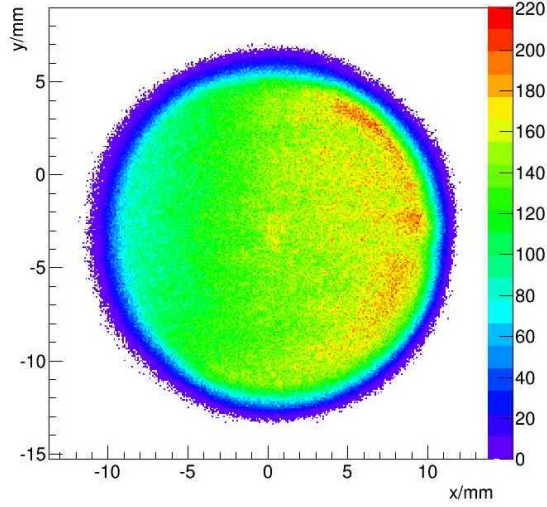


Figure 15: Reconstructed beam position at the target

²⁷⁴ raster magnet current with the beam shape shown in the ADC of the BPMs.
²⁷⁵ Several calibrations were taken during different run periods at a beam current of
²⁷⁶ 100nA using different values of the raster magnet current, as shown in Fig.16(a).

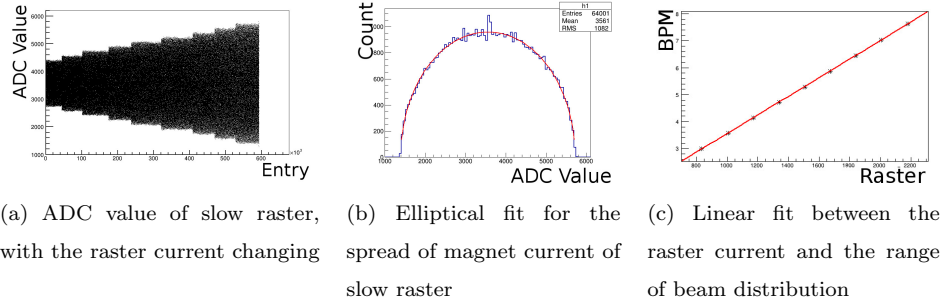


Figure 16: Converting the raster current to beam position shift

²⁷⁷
²⁷⁸ The range of the beam distribution at the target was calculated from the
²⁷⁹ ranges at the two BPMs without applying the filter, using the transport func-
²⁸⁰ tions fitted previously. The range of the beam distribution at the two BPMs
²⁸¹ and the amplitude of the raster current was calculated from an elliptical fit,

²⁸² an example is shown in Fig.16(b). Figure 16(c) shows a linear fit between the
²⁸³ raster current and the range of the beam distribution at the target. The x axis
²⁸⁴ in Fig.16(c) is the magnet current of the raster, and the y axis is the range of
²⁸⁵ the beam distribution obtained from the BPMs.

²⁸⁶ The second method for calibrating the conversion factor used a target called
“carbon hole” as shown in Fig.17(a).

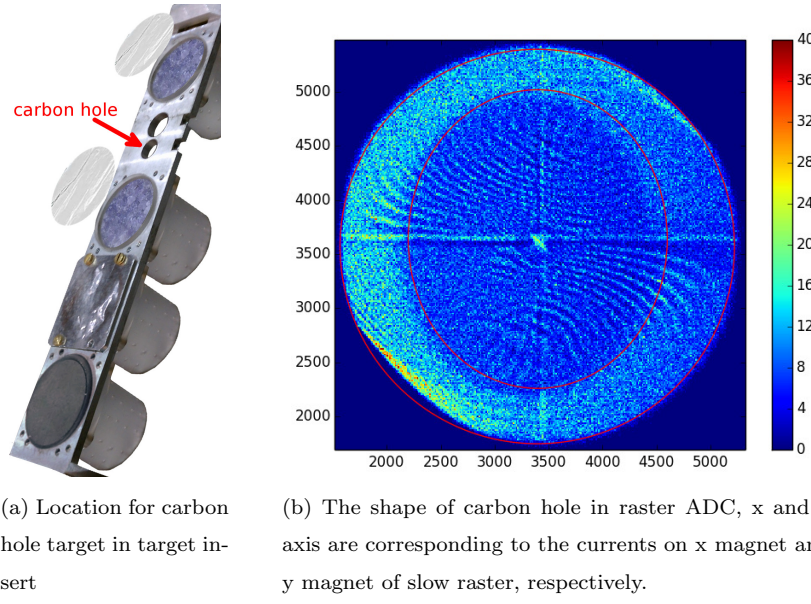


Figure 17: Carbon hole method to calibrate raster

²⁸⁷

²⁸⁸ Scattered electrons were used as the trigger for recording the raster magnet
²⁸⁹ current. Since the density of the target frame was much higher than that of the
²⁹⁰ “hole”, which was submerged in liquid helium, the density of events triggered
²⁹¹ from the target frame was much higher than that of the hole itself. Recorded
²⁹² values reveal a hole shape as shown in Fig.17(b). The size of the carbon hole
²⁹³ was surveyed before the experiment, and a fit program was used to extract the
²⁹⁴ radius of the recorded hole shape for that raster current. The conversion factor
²⁹⁵ F was then calculated as the ratio of the size of the carbon hole S_{hole} and the
²⁹⁶ radius of the hole shape R_{hole} in the ADC:

$$F = \frac{S_{hole}}{2 * R_{hole}}. \quad (14)$$

297 *3.4.2. Conversion factor for the fast raster*

298 The conversion for the fast raster was the same as for the slow raster. The
299 low pass filter for the BPM was set to a higher value than the frequency of the
300 fast raster to see the beam shape at the BPM formed by the fast raster. For a
301 higher frequency filter, a larger beam current was needed to get a clear pattern.
302 The beam current chosen for calibrating the fast raster was near 300 nA, which
303 was the safety limit for the target. The beam shape formed by the fast raster
is shown in Fig.18.

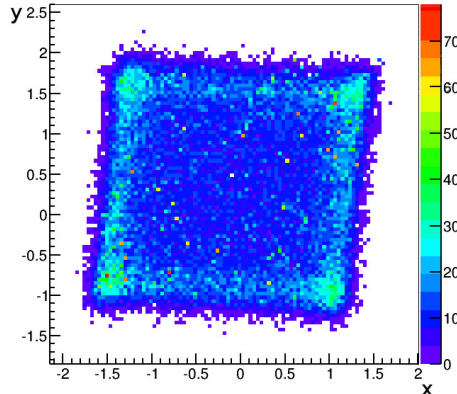


Figure 18: Beam shape formed by the fast raster at the BPM A location, the unit is millimeter

304

305 **4. Uncertainty**

306 The uncertainty of the final beam position at the target for each event con-
307 tains several contributions:

- 308 • The first part comes from the uncertainty of the calibration constant. It
309 includes the BPM resolution for the DAQ runs used for the calibration,
310 the uncertainty of the harp data corresponding to each calibration, and
311 the survey uncertainties for the BPMs and harps. It contributes about 0.7

312 mm for the uncertainty of the position and 0.7 mrad for the uncertainty
313 of the angle.

- 314 • The uncertainty on the pedestal is the largest uncertainty for the beam
315 position measurement, contributing about 0.7~1.5 mm to the uncertainty
316 of the position and 0.7~1.5 mrad to the uncertainty of the angle.
- 317 • The uncertainties from the BPM survey need to be included, since the
318 production data and the calibration data were taken at different beamline
319 settings when the equipment was moved. They contribute 0.5 mm to the
320 uncertainty of the position.
- 321 • The uncertainty from the magnetic field map of the target was considered
322 for the settings with the target magnet field.
- 323 • The uncertainties due to the size conversion of the rasters were also in-
324 cluded.

325 The position uncertainty was magnified by a factor of 5 at the target because of
326 the short distance between the two BPMs. For example, in the straight through
327 setting, if the uncertainty at BPM A is 0.2 mm, and at BPM B is 0.27 mm,
328 the uncertainty at the target is 1.1 mm for position and 1.3 mrad for angle.
329 The uncertainty for the position at the target was around 1~2 mm, while the
330 uncertainty for the angle was 1~2 mrad.

331 5. Summary

332 JLab g2p experiment used a transversely polarized NH_3 target for the first
333 time in Hall A. It put a limit of below 100 nA on the electron beam current and
334 required a slow raster to spread beam to a large area. Two chicane magnets were
335 used to compensate the strong transverse magnetic field. Beam-line equipment,
336 including the BPMs, harps and associated readout system, were upgraded to
337 allow precision measurements of the beam position at low current (50-100 nA).
338 A software filter was used to reduce noise in the BPMs. A corrected equation

339 was used to compensate the non-linearity caused by the diff/sum equation. The
340 harp data and the linear fit between the bpm signal and the beam current were
341 used to extract the calibration constant of the BPM. To account for the strong
342 target magnetic field effect, transport functions were generated to transport the
343 beam position from the BPMs to the target. The beam position in the x-y plane
344 and the angle at the target location are extracted event-by-event by combining
345 information from the BPMs and the signals from the rasters. The performance
346 of the new devices (BPMs, harps and slow rasters) were presented along with
347 an analysis of systematic uncertainties.

348 **Acknowledgments**

349 This work was supported by DOE contract DE-AC05-84ER40150 under
350 which the Southeastern Universities Research Association (SURA) operates the
351 Thomas Jefferson National Accelerator Facility, and by the National Natural
352 Science Foundation of China (11135002, 11275083), the Natural Science Foun-
353 dation of Anhui Education Committee (KJ2012B179).

354 **Reference**

- 355 [1] A. Camsonne, J. P. Chen, D. Crabb and K. Slifer, spokesperson, JLab
356 E08-027 (g2p) experiment. 1
- 357 [2] D. G. Crabb, W. Meyer, Solid polarized targets for nuclear and particle
358 physics experiments, *Annu. Rev. Nucl. Part. Sci.* 47 (1997) 67–109. 1
- 359 [3] R. Michaels, Precision Integrating HAPPEX ADC, JLab Technical report
360 (unpublished).
361 URL [http://hallaweb.jlab.org/parity/prex/adc18/prex_adc18_](http://hallaweb.jlab.org/parity/prex/adc18/prex_adc18_spec.ps)
362 [spec.ps](http://hallaweb.jlab.org/parity/prex/adc18_spec.ps) 2.1
- 363 [4] J. Musson, Functional Description of Algorithms Used in Digital Receivers,
364 JLab Technical report No. JLAB-TN-14-028. 2.1

- 365 [5] C. Yan and et al., Superharp - A wire scanner with absolute position read-
366 out for beam energy measurement at CEBAF, Nuclear Instruments and
367 Methods in Physics Research A 365 (1995) 261–267. 2.2, 3.1
- 368 [6] J. Pierce, J. Maxwell, T. Badman, J. Brock, C. Carlin, D. Crabb, D. Day,
369 C. Keith, N. Kvaltine, D. Meekins, J. Mulholland, J. Shields, K. Slifer,
370 Dynamically polarized target for the and experiments at jefferson lab,
371 Nuclear Instruments and Methods in Physics Research Section A: Acceler-
372 ators, Spectrometers, Detectors and Associated Equipment 738 (0) (2014)
373 54 – 60. doi:<http://dx.doi.org/10.1016/j.nima.2013.12.016>.
374 URL [http://www.sciencedirect.com/science/article/pii/
375 S0168900213016999](http://www.sciencedirect.com/science/article/pii/S0168900213016999) 2.3
- 376 [7] C. Yan, Hall C Polarized Target Raster System Upgrade, JLab Technical
377 report (unpublished).
378 URL https://www.jlab.org/Hall-C/talks/01_06_05/yan.pdf 2.3
- 379 [8] W. . Barry, A general analysis of thin wire pickups for high frequency beam
380 position monitors, Nuclear Instruments and Methods in Physics Research
381 A 301 (1991) 407–416. 3.2
- 382 [9] C.R.Carman, J. L. Pellegrin, The beam positions of the spear storage ring,
383 SLAC-PUB-1227. 3.2
- 384 [10] P.Poit, Evaluation and correction of nonlinear effects in fnpl beam position
385 monitors, FNPL Technical report No.Beams-doc-1894-v1.
386 URL [http://beamdocs.fnal.gov/AD-public/DocDB>ShowDocument?
387 docid=1894](http://beamdocs.fnal.gov/AD-public/DocDB>ShowDocument?docid=1894) 3.2
- 388 [11] R. Wines, private communication. 3.3
- 389 [12] J. Liu, Magnetic field mapping on a translation table, JLab Technical
390 report, E08-027 Collaboration (unpublished).
391 URL [http://hallaweb.jlab.org/experiment/g2p/collaborators/
392 jie/2011_10_05_fieldmap_report/Target_Field_Map_Report.pdf](http://hallaweb.jlab.org/experiment/g2p/collaborators/jie/2011_10_05_fieldmap_report/Target_Field_Map_Report.pdf) 3.3

³⁹³ [13] C. Gu, Target field mapping and uncertainty estimation, JLab Technical
³⁹⁴ report, E08-027 Collaboration (unpublished).
³⁹⁵ URL https://hallaweb.jlab.org/experiment/g2p/collaborators/chao/technotes/Chao_TechNote_TargetField.pdf 3.3
³⁹⁶